Plate-type acoustic metamaterials with strip masses

Felix Langfeldt[1] and Wolfgang Gleine[1]

Department of Automotive and Aeronautical Engineering,

Hamburg University of Applied Sciences, Berliner Tor 7a, D–20099 Hamburg,

Germany[a)]

Plate-type acoustic metamaterials (PAM) consist of a thin plate with periodically added masses. Similar to membrane-type acoustic metamaterials, PAM exhibit anti-resonances at low frequencies at which the transmission loss can be much higher than the mass-law without requiring a pretension. Most PAM designs previously investigated in literature require the addition of up to thousands of masses per square meter. This makes manufacturing of such PAM prohibitively expensive for most applications. In this contribution a much simpler PAM design with strip masses is investigated. An analytical model is derived which can be used to estimate the modal properties, effective mass, and oblique incidence sound transmission loss of PAM with strip masses. For high strip masses (compared to the baseplate), this analytical model can be simplified to yield explicit expressions to directly calculate the resonance and anti-resonance frequencies of such PAM. The analytical model is verified using numerical simulations and laboratory measurement results are presented to demonstrate the performance of PAM with strip masses under diffuse field excitation and finite sample size conditions.

---

a); Felix.Langfeldt@haw-hamburg.de

 This article appeared in: Langfeldt, F. and W. Gleine. Plate-type acoustic metamaterials with strip masses. *The Journal of the Acoustical Society of America* 149(6) (2021): 3737–3738 and may be found at https://doi.org/10.1121/10.0005112.

I. INTRODUCTION

Yang *et al.* (2008) introduced the so-called membrane-type acoustic metamaterials (MAM) as a new class of acoustic metamaterials with lightweight properties and, at the same time, frequency bands in the low-frequency range with remarkably large sound transmission loss (STL) values (considerable larger than the corresponding mass-law). Subsequently, MAM received a lot of attention (e.g. (Huang *et al.*, 2016; Mei *et al.*, 2012; Naify *et al.*, 2011, 2012; Yang *et al.*, 2010)), but one major challenge for the application of MAM in practical noise problems is the pretension of the membrane. The pretension generates the spring stiffness of the unit cell and is therefore critical in determining the vibro-acoustic properties of the metamaterial. In practice, the pretension of a membrane can be difficult to control as it can be subject to relaxation effects in the membrane material or thermal variations. Also, MAM require a relatively heavy frame in order to sustain the pretension and this frame can significantly impair the lightweight properties of MAM. A solution to this problem is to use a plate instead of a membrane as the base material to which the masses are attached. In the case of such plate-type acoustic metamaterials (PAM), the spring stiffness is generated by the bending stiffness of the plate and a pretension is not required (Huang *et al.*, 2016). Several different designs of PAM have been investigated, for example PAM with a frame and no masses in the unit cells (Varanasi *et al.*, 2017), PAM with added masses (Wang *et al.*, 2019), or double-layer PAM with air cavities and orifices (Ang *et al.*, 2018, 2019).

One particular PAM design, which has particularly promising properties for applications with strong weight limitations, consists of a plate with a periodic array of rigid masses attached to the plate and no frame structure at all. In fact, this PAM type has already been investigated by Kurtze (1959) long before the term metamaterial was introduced. More recent research investigated analytically the sound transmission behavior of such PAM (Maysenhölder, 2004), demonstrated their application to the improvement of the low-frequency sound transmission loss of glass wool insulation packages (Langfeldt and Gleine, 2019a), and studied the effect of random inaccuracies in the periodicity of the masses (e.g. due to manufacturing tolerances) (Langfeldt and Gleine, 2020a). Although these PAM exhibit the same low-frequency sound reduction properties as MAM and do not require a pretensioned membrane and frame structure, the large number of masses (typically hundreds or thousands of masses per square meter) lead to a level of complexity which drives the manufacturing cost of such metamaterials to prohibitively high levels—in particular when large surfaces need to be lined with PAM for low-frequency sound insulation. There is therefore a need for PAM designs with similar beneficial acoustic properties in the low-frequency range, but greatly reduced complexity to enable industrial manufacturing at reasonable cost. In this contribution, a novel PAM design is proposed in which the small masses are replaced by long strips. Thus, the number of masses to be attached to the baseplate is greatly reduced and it will be shown that an improved sound transmission loss at low-frequencies can be achieved even with such a simplified setup. Liu and Du (2019) investigated a similar membrane-type acoustic metamaterial with strip masses, but they only considered the MAM as part of the wall of a duct system and did not investigate the sound transmission through the metamaterial itself.

The present contribution is structured as follows: First, an analytical model for the prediction of the sound transmission loss of PAM with strip masses is presented. Compared to previous models, the proposed analytical model does not require the solution of linear systems of equations and, apart from a transcendental equation to obtain the eigenfrequencies of the PAM, provides only explicit expressions to obtain all necessary quantities for the calculation of the PAM sound transmission loss. In fact, it will be shown that for large strip masses the model can be significantly simplified to obtain expressions that can be directly used to estimate the vibro-acoustic properties of PAM designs. To the knowledge of the authors, this is the first time such expressions are proposed for acoustic metamaterials of this kind. In section III, the proposed analytical model is verified using numerical simulations. Furthermore, simulations are employed to investigate (1) the accuracy of the analytical model when applied to PAM under oblique incidence excitation and (2) the limitation of the assumption of rigid strip masses in the analytical model. Sound transmission loss measurement results for a PAM with strip masses are presented in section IV in order to demonstrate the effectiveness of the novel PAM design even when a finite sized sample and diffuse sound field excitation are considered. The experimental results are compared to predictions obtained from the analytical model in section II. Finally, the paper is concluded with a brief summary of the key findings and a discussion of practical implications for the application of PAM with strip masses.

II. ANALYTICAL MODEL

A number of analytical models for the prediction of the sound transmission loss of PAM can be found in the literature. For example, Maysenhölder (1998) presented an analytical model for calculating the sound transmission loss of periodically inhomogeneous plates using a Fourier expansion of the inhomogeneous plate properties. In (Chen *et al.*, 2014; Langfeldt and Gleine, 2019b) the point matching approach is used to couple the baseplate with arbitrarily shaped masses and obtain the modal and sound transmission properties of PAM unit cells. In (Liu *et al.*, 2019) the same method is applied specifically to MAM with strip masses. Although these analytical models could in principle be adapted and applied to the PAM with strip masses, all these models have in common that they rely on the truncation of infinite series expansions which results in relatively large linear systems of equations that need to be solved for each metamaterial design.

In this section, the simple structure of the PAM with strip masses will be exploited to derive explicit expressions for calculating the sound transmission loss. These expressions can be readily applied to design and optimize unit cells of PAM with strip masses. In section II A, the basic geometrical and material property definitions of the PAM are introduced. The analytical model to obtain the effective surface mass density of a PAM unit cell is derived in section II B. Finally, in section II C this model is further simplified for high strip masses, yielding very simple expressions to directly calculate the modal properties of the PAM unit cell.

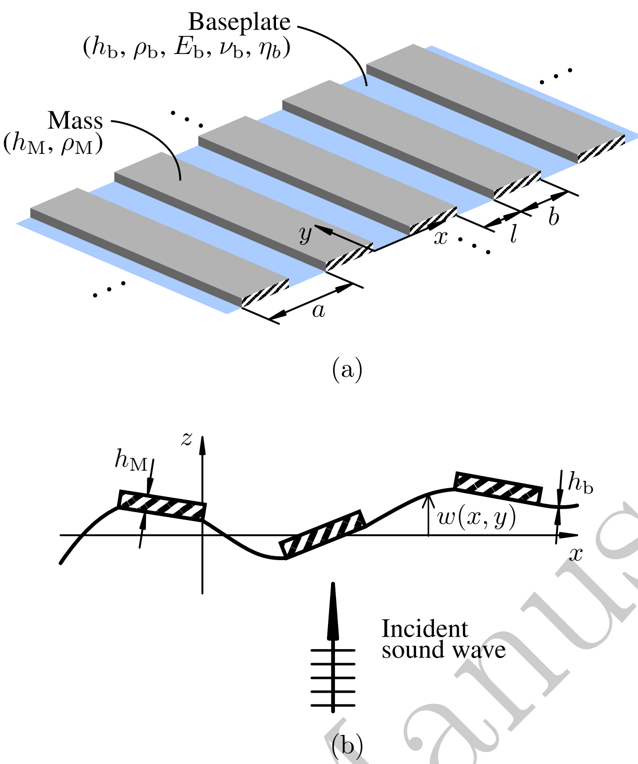

FIG. 1. (Color online) Basic geometrical structure of a part of a plate-type acoustic metamaterial (PAM) with strip masses. (a) Isometric view. (b) Cross-sectional view with an illustration of the transversal displacement $w(x, y)$ due to an incident sound wave.

A. Definitions

Figure 1(a) shows an isometric view of the basic structure of the PAM. It consists of a homogeneous baseplate with a thickness of h_b. The material of the baseplate is characterized by the density ρ_b, Young's modulus E_b, Poisson's ratio ν_b, and structural loss factor η_b. Strip masses are attached periodically onto the baseplate. The width of the strips is specified by the parameter b and the spacing between each mass is denoted l. Thus, the size of a unit cell of the PAM is given by $a = b + l$. It is assumed that the flexural rigidity of the masses is much higher than that of the baseplate. Therefore, in order to simplify the analysis, they can be considered as rigid bodies fully characterized by the thickness h_{M} and density ρ_{M}. Based on the structure shown in Figure 1(a), the total surface mass density of the PAM is

$$m_0'' = m_{\mathrm{b}}'' + \frac{b}{a} m_{\mathrm{M}}'' = \rho_{\mathrm{b}} h_{\mathrm{b}} + \frac{b}{a} \rho_{\mathrm{M}} h_{\mathrm{M}}. \tag{1}$$

A Cartesian coordinate system is defined with the x-axis being on the midsurface of the baseplate and perpendicular to the spanwise direction of the masses. The y-axis points along the edge of one strip mass and the z-axis, consequently, is oriented normally to the baseplate. The dots in Figure 1(a) indicate that the PAM is extending infinitely within the xy-plane.

Throughout this contribution, a harmonic time-dependence of the form $\exp(\mathrm{i}\omega t)$ (with $\mathrm{i} = \sqrt{-1}$, the angular frequency ω, and the time t) is implicitly assumed.

B. Effective surface mass density

The effective material properties of an acoustic metamaterial can be used to determine the sound transmission properties in the low-frequency range (i.e. frequencies for which the acoustic wavelength is larger than the unit cell size of the metamaterial). Several methodologies for the homogenization of acoustic metamaterials exist in the literature (Fokin *et al.*, 2007; Terroir *et al.*, 2019; Yang *et al.*, 2014). Since only the far-field transmission of sound through the PAM is of interest here and the PAM are much thinner than the acoustic wavelength, the Green's function based one-dimensional homogenization method by Yang *et al.* (2014) will be employed. As explained in more detail in (Langfeldt and Gleine, 2020b), for thin plate-type acoustic metamaterials with unconstrained unit cell edges this homogenization procedure can be expressed in terms of a modal expansion of the effective surface mass density m''_{eff} as

$$m''_{\text{eff}} = m''_0 \left(1 - \sum_{i=1}^{N} \frac{1}{\mu_i} \frac{\omega^2}{\omega_i^2(1+\mathrm{i}\eta) - \omega^2}\right)^{-1} \tag{2}$$

with the mode index i, the number of non-zero eigenmodes N to be considered in the expansion, the angular eigenfrequency ω_i, and the structural loss factor of the PAM material η. The normalized modal masses μ_i are given by

$$\mu_i = \frac{1}{m''_0 S} \frac{\int_\Omega \rho \mathbf{u}_i{}^H \mathbf{u}_i \,\mathrm{d}\Omega}{|\langle w_i \rangle|^2}, \tag{3}$$

where S is the area of a PAM unit cell, Ω represents the domain of the unit cell (including the baseplate and the strip mass), $\mathbf{u}_i$ is the modal displacement vector field, $\mathbf{u}_i{}^H$ is the Hermitian transpose of $\mathbf{u}_i$, and $\langle w_i \rangle$ is the surface-averaged transversal PAM displacement averaged over the unit cell S (Langfeldt and Gleine, 2020b). Therefore, to determine the effective surface mass density according to Equation 2, the relevant eigenfrequencies and mode shapes of the PAM unit cell need to be known.

It should be noted that the effective surface mass density (or effective density, which is directly related to m''_{eff} via the metamaterial thickness) has been successfully applied to evaluate the far field sound transmission of acoustic metamaterials. For example, in (Yang *et al.*, 2008) this concept was used to analyze and explain the sound transmission behavior of MAM. Closely related methods have also been applied to other kinds of metamaterial plates (e.g. (de Melo Filho *et al.*, 2019; Langfeldt and Gleine, 2019b; Xiao *et al.*, 2021, 2012)). Because the present work is focused on the sound transmission through PAM with strip masses, the effective surface mass density therefore is a suitable and established method for modeling this phenomenon. There are, on the other hand, numerous models and investigations available in the literature that are based on a more general mathematical basis, e.g. the Bloch-Floquet theory (see, for example, (Antonakakis and Craster, 2012; Craster *et al.*, 2010; Maysenhölder, 1998)). These models also enable, for example, the calculation of wave propagation properties (such as dispersion curves) and can be applicable to higher frequencies with wavelengths comparable to the unit cell size. However, since the low-frequency sound transmission loss is of main interest here, the effective surface mass density based approach is followed.

In order to simplify the analysis, the vibro-acoustic response of the PAM unit cell to a normally incident plane acoustic wave is considered here. The effect of obliquely incident plane waves will be discussed in section III B. Figure 2 provides an illustrative example showing the simulated displacement of a part of a PAM with strip masses excited by a normally incident plane acoustic wave. Due to the symmetry of the PAM and the exciting sound field, the displacement field in y-direction is constant and the vibration of a PAM unit cell can be simplified to the two-dimensional setup in the xz-plane, as illustrated at the bottom of Figure 2. In this case, the displacement field $w(x, y)$ of the PAM can be subdivided into two parts: The part covered by the strip mass ($x \in [l, a]$) undergoes a translational rigid body motion with the amplitude W_{M}, because the bending stiffness of the mass is considerably larger than that of the baseplate. The other part consists of the baseplate between the mass strips and is governed by the partial differential equation

$$-m''_{\mathrm{b}}\omega^2 w + D_{\mathrm{b}}\left(\frac{\partial^4 w}{\partial x^4} + 2\frac{\partial^4 w}{\partial x^2 \partial y^2} + \frac{\partial^4 w}{\partial y^4}\right) = \Delta p, \tag{4}$$

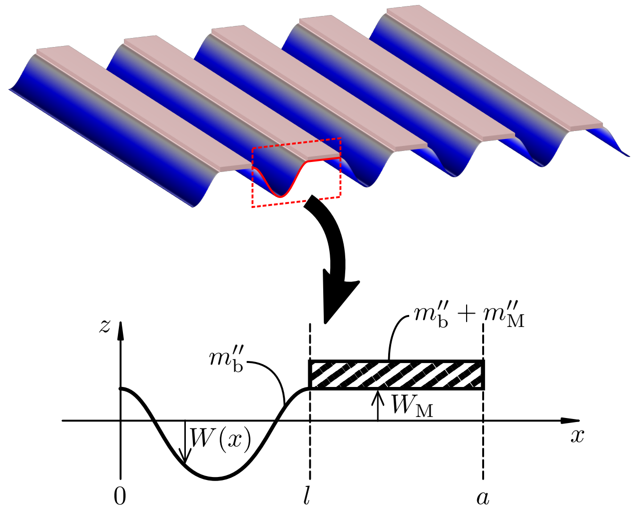

FIG. 2. (Color online) Displacement of a part of a PAM with strip masses excited by a normally incident plane wave.

where $D_{\mathrm{b}} = E_{\mathrm{b}} h_{\mathrm{b}}^3/(12(1-\nu_{\mathrm{b}}^2))$ is the bending stiffness of the baseplate and Δp is the acoustic excitation of the PAM (Ventsel and Krauthammer, 2001). Due to the essentially two-dimensional character of the PAM vibration, the spatial derivatives in y-direction vanish in Equation 4. The mode shape functions $W_i(x)$ of the baseplate in between the mass strips fulfill the homogeneous variant of Equation 4, which simplifies to the boundary value problem

$$-\kappa_i^4 W_i + \frac{\partial^4 W_i}{\partial x^4} = 0, \tag{5}$$

where $\kappa_i = \sqrt{\sqrt{12}\omega_i/(h_{\mathrm{b}} c_{\mathrm{b}})}$ has been defined and $c_{\mathrm{b}} = \sqrt{E_{\mathrm{b}}/(\rho_{\mathrm{b}}(1-\nu_{\mathrm{b}}^2))}$ is the quasi-longitudinal wave velocity in the baseplate material. As shown in the bottom sketch in Figure 2, Equation 5 is subject to the boundary conditions

$$\begin{aligned} &W_i(0) = W_i(l) = W_{\mathrm{M},i} \\ \text{and} \quad &\left.\frac{\partial W_i}{\partial x}\right|_{x=0} = \left.\frac{\partial W_i}{\partial x}\right|_{x=l} = 0, \end{aligned} \tag{6}$$

where $W_{\mathrm{M},i}$ is the mode shape component of the mass that is dynamically coupled to the baseplate via Newton's second law of motion:

$$-\omega_i^2 b(m''_{\mathrm{b}} + m''_{\mathrm{M}})W_{\mathrm{M},i} = -2D_{\mathrm{b}} \frac{\partial^3 W_i}{\partial x^3}\bigg|_{x=l}. \tag{7}$$

It should be noted that the left hand side in Equation 7 corresponds to the inertia of the strip mass and the baseplate material covered by the strip mass. The left hand side represents the transversal interface forces in the baseplate acting on both sides of the strip mass. Equation 7 can be solved for $W_{\mathrm{M},i}$ as follows:

$$W_{\mathrm{M},i} = \frac{2}{\kappa_i^4 b(1+\mu)} \frac{\partial^3 W_i}{\partial x^3}\bigg|_{x=l}, \tag{8}$$

with the mass ratio $\mu = m''_{\mathrm{M}}/m''_{\mathrm{b}}$.

The solutions to the boundary value problem in Equation 5 can be expressed in the following form (Rao, 2007):

$$W_i(x) = A_i\alpha(\kappa_i x) + B_i\beta(\kappa_i x) + C_i\gamma(\kappa_i x) + D_i\delta(\kappa_i x), \tag{9}$$

with

$$\begin{aligned} \alpha(\kappa_i x) &= \cos(\kappa_i x) + \cosh(\kappa_i x), \\ \beta(\kappa_i x) &= \cos(\kappa_i x) - \cosh(\kappa_i x), \\ \gamma(\kappa_i x) &= \sin(\kappa_i x) + \sinh(\kappa_i x), \\ \text{and} \quad \delta(\kappa_i x) &= \sin(\kappa_i x) - \sinh(\kappa_i x). \end{aligned} \tag{10}$$

In conjunction with the boundary conditions in Equation 6 as well as Equation 8, this leads to the homogeneous system of equations

$$\begin{pmatrix} 1 & 0 & 0 & \frac{\mathcal{C}}{\kappa_i l} \\ 0 & 0 & \kappa_i & 0 \\ \alpha(\kappa_i l) & \beta(\kappa_i l) & \gamma(\kappa_i l) & \delta(\kappa_i l) + \frac{2\mathcal{C}}{\kappa_i l} \\ -\kappa_i\delta(\kappa_i l) & -\kappa_i\gamma(\kappa_i l) & \kappa_i\alpha(\kappa_i l) & \kappa_i\beta(\kappa_i l) \end{pmatrix} \begin{pmatrix} A_i \\ B_i \\ C_i \\ D_i \end{pmatrix} = \begin{pmatrix} 0 \\ 0 \\ 0 \\ 0 \end{pmatrix}, \tag{11}$$

where the constant $\mathcal{C} = 2l/(b(1+\mu))$ has been introduced. The eigenfrequencies ω_i can be determined by computing the values of κ_i for which the determinant of the system matrix in Equation 11 vanishes. This leads to the characteristic equation

$$1 - \cos(\kappa_i l)\cosh(\kappa_i l) = \mathcal{C}\frac{(\cos(\kappa_i l) - 1)\sinh(\kappa_i l) + (\cosh(\kappa_i l) - 1)\sin(\kappa_i l)}{\kappa_i l}. \tag{12}$$

Equation 12 can be solved numerically for $\kappa_i l$, which then allows the computation of the eigenfrequencies via the relationship

$$\omega_i = \frac{h_\mathrm{b} c_\mathrm{b}}{\sqrt{12} l^2}(\kappa_i l)^2. \tag{13}$$

For each eigenfrequency ω_i the coefficients A_i, B_i, C_i, and D_i in Equation 9 are given by

$$\begin{aligned} A_i &= -\frac{\mathcal{C}}{\kappa_i l} D_i \\ B_i &= \frac{2 - \alpha(\kappa_i l)}{\beta(\kappa_i l)} A_i - \frac{\delta(\kappa_i l)}{\beta(\kappa_i l)} D_i, \\ \text{and} \quad C_i &= 0. \end{aligned} \tag{14}$$

Inserting this into Equation 9 yields the following mode shape function for the baseplate between the mass strips

$$W_i(x) = \left(\delta(\kappa_i x) - \frac{\delta(\kappa_i l)}{\beta(\kappa_i l)}\beta(\kappa_i x) - \frac{\mathcal{C}}{\kappa_i l}\left(\alpha(\kappa_i x) - \frac{2 - \alpha(\kappa_i l)}{\beta(\kappa_i l)}\beta(\kappa_i x)\right)\right) D_i \tag{15}$$

and the modal displacement amplitude of the mass follows from Equation 8 as

$$W_{\mathrm{M},i} = 2A_i = -\frac{2\mathcal{C}}{\kappa_i l} D_i. \tag{16}$$

Equation 15 and Equation 16 are used to obtain the normalized modal mass μ_i, according to the definition in Equation 3. Because of the periodicity and the (at the assumed normal incidence) constant displacement in y-direction, the surface-averaged transversal PAM displacement appearing in the denominator of Equation 3 can be obtained from integrating the mode shape function of the PAM over one unit cell in the x-direction:

$$\langle w_i \rangle = \frac{1}{a} \int\limits_0^a w_i(x,0)\,\mathrm{d}x = \frac{1}{a} \left(\int\limits_0^l W_i(x)\,\mathrm{d}x + bW_{\mathrm{M},i} \right). \tag{17}$$

For the same reasons, the density-weighted integral of the squared magnitude of the displacement amplitude can be rewritten with a one-dimensional integral as follows:

$$\frac{1}{m_0'' S} \int\limits_\Omega \rho {\mathbf{u}_i}^H \mathbf{u}_i \,\mathrm{d}\Omega = \frac{1}{a} \frac{m_\mathrm{b}''}{m_0''} \left(\int\limits_0^l W_i(x)^2\,\mathrm{d}x + b(1+\mu) W_{\mathrm{M},i}^2 \right). \tag{18}$$

After inserting Equation 15 and Equation 16 and performing the integrations, the following expression for μ_i results:

$$\mu_i = \frac{m_\mathrm{b}''}{m_0''} \frac{a}{l} \kappa_i l \frac{J_{11}A_i^2 + J_{12}A_iB_i + J_{14}A_iD_i + J_{22}B_i^2 + J_{24}B_iD_i + J_{44}D_i^2}{(I_1A_i + I_2B_i + I_4D_i)^2}, \tag{19}$$

which, for clarity, has been written in compact form with the coefficients given by

$$
\begin{aligned}
I_1 &= \gamma(\kappa_i l) + 2\kappa_i l\left(\frac{a}{l} - 1\right),\\
I_2 &= \delta(\kappa_i l),\\
I_4 &= 2 - \alpha(\kappa_i l),\\
J_{11} &= \kappa_i l + 8\frac{\kappa_i l}{\mathcal{C}} + \frac{3\alpha(\kappa_i l)\gamma(\kappa_i l) - \beta(\kappa_i l)\delta(\kappa_i l))}{4},\\
J_{12} &= \frac{\alpha(\kappa_i)\delta(\kappa_i l) + \beta(\kappa_i l)\gamma(\kappa_i l)}{2},\\
J_{14} &= 4 - \alpha(\kappa_i l)^2,\\
J_{22} &= \kappa_i l - \frac{\alpha(\kappa_i l)\gamma(\kappa_i l) - 3\beta(\kappa_i l)\delta(\kappa_i l))}{4},\\
J_{24} &= \delta(\kappa_i l)^2, \text{ and}\\
J_{44} &= \frac{\beta(\kappa_i l)\gamma(\kappa_i l) - 3\alpha(\kappa_i l)\delta(\kappa_i l))}{4}.
\end{aligned}
\tag{20}
$$

It should be noted that in Equation 19 the indeterminate constant D_i will cancel out in both the numerator and denominator, so that the value of μ_i will be independent of the eigenvector scaling.

In summary, the procedure for calculating the sound transmission loss of a given PAM with strip masses using the proposed analytical model is as follows:

1. Numerically solve Equation 12 for the first N positive roots $\kappa_i l$.
2. Calculate the corresponding eigenfrequencies ω_i using Equation 13.
3. Calculate the normalized modal masses μ_i using Equation 19 in conjunction with Equation 14 and Equation 20.
4. Calculate the effective surface mass density m''_{eff} of the PAM via Equation 2.

5. Calculate the sound transmission loss TL with m''_{eff} substituted into the mass-law formula:

$$\mathrm{TL} = 20\lg\left|1 + \frac{\mathrm{i}\omega m''_{\text{eff}}\cos\theta_0}{2\rho_0 c_0}\right|. \tag{21}$$

In most cases the first anti-resonance frequency f_{P1} is of main concern and only the first positive eigenfrequency of the PAM unit cell needs to be considered ($N = 1$). Consequently, the effective surface mass density is given by

$$m''_{\text{eff}} = m''_0\left(1 - \frac{\omega^2}{(1+\mu_1)\omega^2 - \mu_1\omega_1^2(1+\mathrm{i}\eta)}\right) \tag{22}$$

and the anti-resonance frequency f_{P1} corresponds to the pole of Equation 22 at which $m''_{\text{eff}} \to \infty$ (undamped case with $\eta = 0$):

$$f_{\text{P1}} = \sqrt{\frac{\mu_1}{1+\mu_1}}\frac{\omega_1}{2\pi}. \tag{23}$$

C. Simplified equations for $\mathcal{C} \ll 1$

If the surface mass density of the strip masses m''_{M} is considerably larger than the baseplate surface mass density m''_{b}, the constant $\mathcal{C}$ can be much smaller than unity. According to Equation 16, this results in a near-zero displacement amplitude of the strip mass at the PAM eigenmodes. Figure 3(a) shows the value of the first positive root of Equation 12 for different values of $\mathcal{C}$. This diagram shows that if $\mathcal{C} \ll 1$, then $\kappa_1 l$ will asymptotically approach the first positive root for the special case $\mathcal{C} = 0$, corresponding to a PAM with fixed strip masses. For this special case, the characteristic equation in Equation 12 will simplify to

$$1 - \cos(\kappa_i l)\cosh(\kappa_i l) = 0 \tag{24}$$

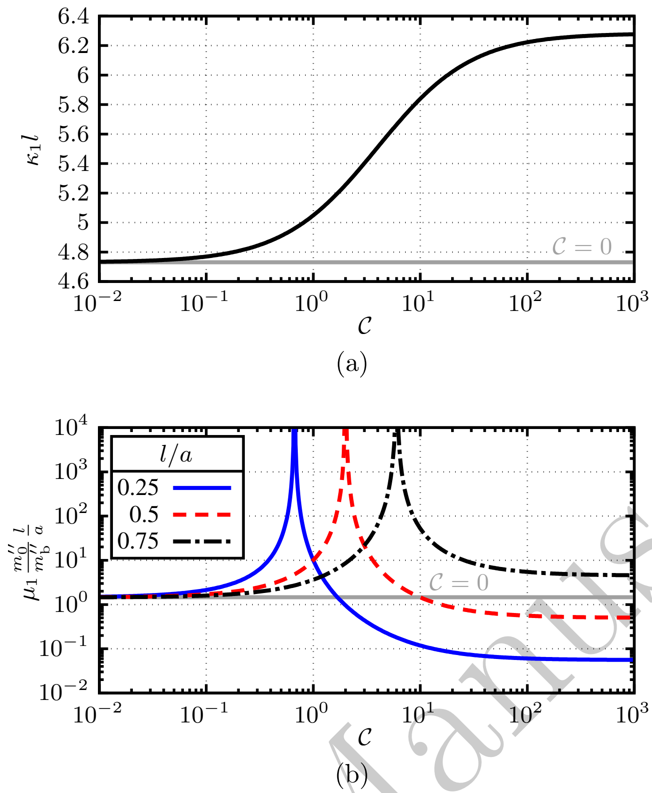

FIG. 3. (Color online) Variation of the modal parameters for the first positive eigenmode of a PAM unit cell for different values of the constant $\mathcal{C}$. (a) First root of Equation 12. (b) Associated normalized modal mass (Equation 19).

and the baseplate mode shape function is given by

$$W_i(x) = \left(\delta(\kappa_i x) - \frac{\delta(\kappa_i l)}{\beta(\kappa_i l)}\beta(\kappa_i x)\right) D_i, \tag{25}$$

corresponding to the characteristic equation and mode shape of a beam with both ends clamped (Rao, 2007). Using Equation 25, the normalized modal mass μ_i reduces for $\mathcal{C} = 0$ to

$$\mu_i = \frac{m_\mathrm{b}''}{m_0''}\frac{a}{l}\left(\frac{\kappa_i l \delta(\kappa_i l)}{2\beta(\kappa_i l) + \frac{1}{2}(\gamma(\kappa_i l)^2 - \delta(\kappa_i l)^2)}\right)^2. \tag{26}$$

The first positive root of Equation 24 is given by $\kappa_1 l \approx 4.73$. Thus, the first resonance frequency is approximately

$$\omega_1 = \frac{h_\mathrm{b} c_\mathrm{b}}{\sqrt{12} l^2} (\kappa_1 l)^2 \approx 6.458 \frac{h_\mathrm{b} c_\mathrm{b}}{l^2} \tag{27}$$

and the normalized modal mass associated with this eigenmode is

$$\mu_1 \approx 1.449 \frac{m''_\mathrm{b}}{m''_0} \frac{a}{l}. \tag{28}$$

Equation 27 and Equation 28 are explicit expressions for the modal properties of the first mode of a PAM with strip masses that are much heavier than the baseplate. These expressions can be used directly to estimate the sound transmission loss of the PAM via the effective surface mass density determined using Equation 2. These equations also clearly show how the modal parameters can be tuned: The resonance frequency is directly proportional to the baseplate thickness and the longitudinal wave velocity of the baseplate material. It is also inversely proportional to the square of the distance between mass strips l. The normalized modal mass, on the other hand, is directly proportional to m''_b/m''_0 as well as the unit cell size a. Furthermore, μ_1 is inversely proportional to l.

The effect of $\mathcal{C}$ on the normalized modal mass μ_1 of the first positive PAM eigenmode is shown in Figure 3(b) for different values of the relative mass spacing l/a. It should be noted that in this diagram μ_1 has been scaled by $m''_0 a/(m''_\mathrm{b} l)$ in order to more clearly show that μ_1 asymptotically approaches the value given by Equation 28, as $\mathcal{C} \to 0$. Apart from this asymptotic behavior of μ_1 for small values of $\mathcal{C}$, it can be seen that the normalized modal mass has a pole at a certain value of $\mathcal{C}$ that depends on the value of l/a. μ_1 becomes infinitely large if the surface-averaged modal displacement amplitude $\langle w_i \rangle$ becomes zero.

This is the case when the modal displacement of the strip mass $W_{\mathrm{M},i}$ exactly cancels out the average displacement of the baseplate material not covered by the masses. Consequently, the incident sound waves do not couple with this PAM eigenmode and the mode therefore does not contribute to any anti-resonances of the PAM. Very high values of μ_i should therefore be avoided, if significant PAM anti-resonances are desired. Beyond the pole at very high values of $\mathcal{C}$, the normalized modal mass asymptotically approaches another value that depends on the value of l/a (larger values of l/a leading to larger asymptotic values).

III. NUMERICAL SIMULATIONS

The simulation model of the PAM unit cell is shown in Figure 4. It consists of a two-dimensional mesh in the xz-plane discretizing the baseplate, one strip mass and the fluid on both sides of the PAM. The fluid domains are truncated using perfectly matched layers (PML) in order to minimize reflections of sound waves at these boundaries. At the sides of the computational domain Bloch-Floquet periodic boundary conditions are prescribed so that the unit cell is modeled as part of an infinite periodic array. In the out-of-plane direction (y-axis), the acoustic pressure and solid displacements are modeled with an out-of-plane expansion of the form $\exp(-\mathrm{i}k_{0,y}y)$, in order to simulate an infinitely extending metamaterial in the y-direction. The PAM is excited by a plane acoustic wave with Cartesian wave number components $k_{0,x} = k_0 \sin\theta_0 \cos\phi_0$, $k_{0,y} = k_0 \sin\theta_0 \sin\phi_0$, and $k_{0,z} = k_0 \cos\theta_0$. The acoustic wave number is given by $k_0 = \omega/c_0$. The resulting sound transmission loss is evaluated by integrating the sound intensity at the transmission side of the PAM to obtain the radiated

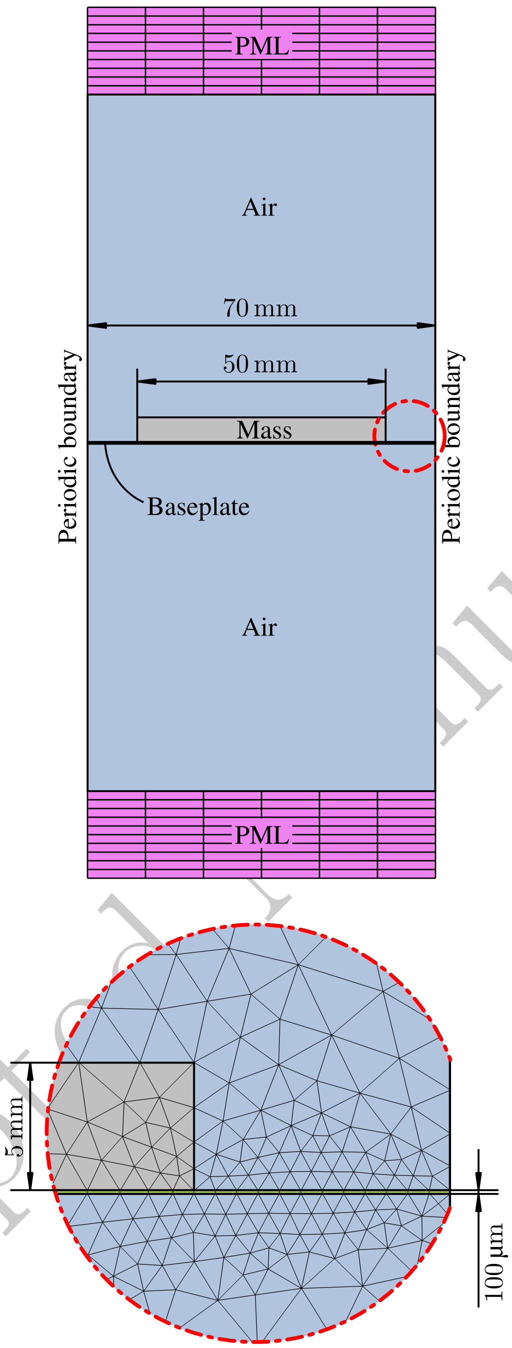

FIG. 4. (Color online) Illustration of the geometry, boundary conditions, and mesh of the two-dimensional FEM simulation model of the PAM unit cell.

TABLE I. Material parameters of the baseplate and mass used in the analytical calculations and numerical simulations.

	Baseplate	Mass
Material	PET	PVC-F
Density ($\mathrm{kg\,m^{-3}}$)	1400	460
Young's modulus (MPa)	3500	1200
Poisson's ratio (—)	0.4	0.4
Longitudinal wave velocity ($\mathrm{m\,s^{-1}}$)	1725	1762
Loss factor (%)	10	10

sound power W_{rad}. The incident sound power W_{inc} is determined from the incident sound wave and the sound transmission loss can then be calculated via $\mathrm{TL} = -10\,\mathrm{lg}(W_{\mathrm{rad}}/W_{\mathrm{inc}})$.

The PAM unit cell design considered here consists of a $h_{\mathrm{b}} = 100\,\mu\mathrm{m}$ thick baseplate made of polyethylene terephthalate (PET). The material of the strip masses is a closed-cell polyvinyl chloride foam (PVC-F) with a thickness of $h_{\mathrm{M}} = 5\,\mathrm{mm}$. The mechanical properties of the materials that were used in the simulations are given in Table I. From this it follows that $m''_{\mathrm{b}} = 140\,\mathrm{g\,m^{-2}}$, $m''_{\mathrm{M}} = 2.3\,\mathrm{kg\,m^{-2}}$, and therefore $\mu = m''_{\mathrm{M}}/m''_{\mathrm{b}} = 16.4$. The unit cell size is $a = 70\,\mathrm{mm}$ and the width of the mass strips is given by $b = 50\,\mathrm{mm}$, which results in $l = a - b = 20\,\mathrm{mm}$. Consequently, $\mathcal{C} \approx 0.046$ is very small and Equation 27 and Equation 28 should provide a reasonable estimate of the modal properties for the first eigenmode of the

PAM unit cell. The total surface mass density of the PAM is given by $m_0'' = 1.8\,\mathrm{kg\,m^{-2}}$ and the density and speed of sound of the fluid are given by $\rho_0 = 1.2\,\mathrm{kg\,m^{-3}}$ and $c_0 = 343\,\mathrm{m\,s^{-1}}$, respectively.

A detailed view of the mesh used in the finite element simulations is provided at the bottom of Figure 4. The cross-section of the baseplate was discretized using second-order quadrilateral elements, with one element in through-thickness direction and 12 elements on each part of the baseplate not covered by the mass. For the mass and the fluid, second-order triangular elements were used with a maximum element size of $a/6 \approx 12\,\mathrm{mm}$. In each of the PML, 10 layers were applied to ensure minimized reflections at these boundaries. The linear system of equations resulting from this discretization was solved using a direct solver for frequencies from $f = 100$ to $1000\,\mathrm{Hz}$.

In the calculations using the analytical model, only the first non-zero eigenmode of the PAM unit cell (defined by f_1 and μ_1) is considered in Equation 2. The reason for this is that the main focus is the first anti-resonance of the metamaterial which is primarily governed by the first non-zero eigenmode. To account for damping, η is replaced in Equation 2 by the structural loss factor of the baseplate material (see Table I). The effective surface mass density approach is only valid as long as the acoustic wavelength is much larger than the size of the unit cells (Yang *et al.*, 2008). At the highest considered frequency (1000 Hz) the wavelength is 0.34 m, which is nearly 5 times larger than the unit cell size of the PAM. Therefore, this assumption is valid for the interpretation of the analytical results.

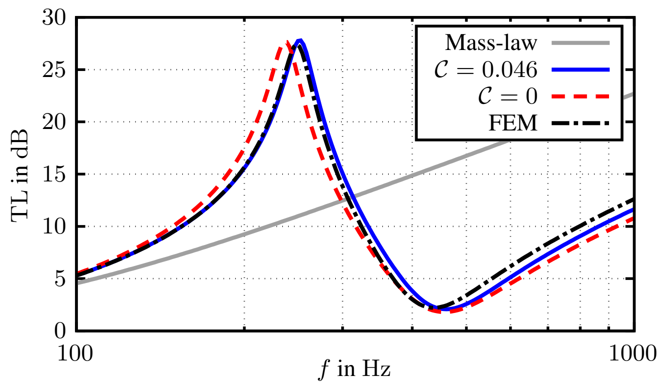

FIG. 5. (Color online) Comparison of analytical and numerical results for the normal incidence sound transmission loss of the PAM.

A. Verification of the analytical model

In order to verify the analytical model in section II, simulation results obtained for normal incidence ($\theta_0 = 0$) are used. Figure 5 shows a comparison between the analytical results (obtained using the more accurate model in section II B with $\mathcal{C} = 0.046$ and the simplified model in section II C with $\mathcal{C} = 0$) and the results of the numerical simulations. As a reference, the grey curve in Figure 5 indicates the STL of a homogeneous plate with equal total surface mass density, according to the mass-law. In general, all three PAM curves in Figure 5 are very similar with an anti-resonance at approximately 250 Hz with sound transmission loss values over 25 dB. At higher frequencies, the PAM transmission loss exhibits a dip at the resonance frequency around 450 Hz and then the STL values remain about 11 dB below the mass-law curve due to the decoupling of the strip masses from the baseplate. A direct comparison of the two analytical results with the FEM data shows that the more accurate model with $\mathcal{C} = 0.046$ indeed yields results that are closer to the simulations than in the simplified case. In the simulation results, the anti-resonance frequency appears at 248 Hz.

TABLE II. Comparison of the numerical and analytical results for the first positive eigenfrequency f_1, normalized modal mass μ_1, and anti-resonance frequency f_{P1} of the PAM unit cell.

	FEM	$\mathcal{C} = 0.046$		$\mathcal{C} = 0$	
f_1 (Hz)	450	447	($-0.7\,\%$)	443	($-1.6\,\%$)
μ_1 (—)	0.462	0.462	($0\,\%$)	0.398	($-13.9\,\%$)
f_{P1} (Hz)	248	251	($+1.2\,\%$)	237	($-4.4\,\%$)

The analytical model predicts the anti-resonance to be at 251 Hz (for $\mathcal{C} = 0.046$) and 237 Hz ($\mathcal{C} = 0$). Therefore, even with the simplified analytical model the anti-resonance frequency can be predicted with an error of less than 5 %—well inside typical uncertainty margins due to other parameters of the PAM, such as the material properties or the geometrical dimensions.

A more comprehensive overview of the accuracy of the analytical model in terms of the modal properties and the anti-resonance frequency is provided in Table II. This shows that the modal properties (f_1 and μ_1) resulting from the analytical model with $\mathcal{C} = 0.046$ are very close to the modal values obtained from a numerical modal analysis of the PAM simulation model. Therefore, the anti-resonance frequency f_{P1} also is quite close to the simulated result. On the other hand, if $\mathcal{C} = 0$, the normalized modal mass μ_1 is considerably underestimated which results in a larger error in the predicted anti-resonance frequency, even though the first resonance frequency is quite accurate ($-1.6\,\%$ error). Nevertheless, as mentioned above, for both variants of the analytical models, the accuracy with respect to the FEM solution

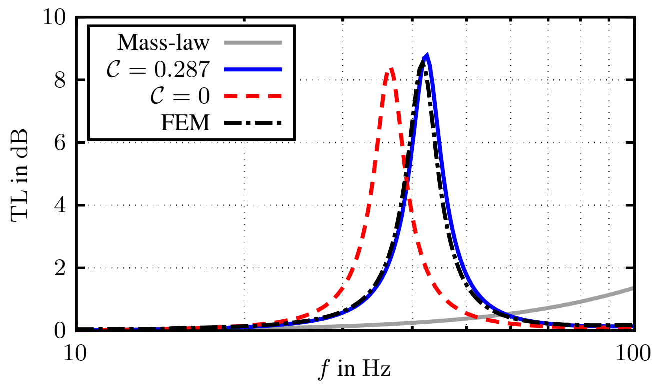

FIG. 6. (Color online) Comparison of analytical and numerical results for the normal incidence sound transmission loss of a PAM with a smaller strip mass ($b = 20\,\mathrm{mm}$).

is well within acceptable bounds so that the model can be regarded as validated for these types of PAM.

It is important to note that $\mathcal{C}$ not only depends on the mass ratio μ, but it is also proportional to l/b. This means that even when μ is very large, $\mathcal{C}$ can be considerably greater than zero if the strip masses cover only a small part of the unit cells (and l/b is large). This is illustrated in Figure 6, which shows analytical and numerical results for a PAM with the same properties as the PAM shown in Figure 4, except for a much smaller mass width of $b = 20\,\mathrm{mm}$ (note the reduced frequency range between 10 and 100 Hz). In this case, the value of $\mathcal{C}$ is 0.287 and it can be clearly seen that the simplified model with $\mathcal{C} = 0$ is not applicable, even though $\mu \gg 1$.

B. Effect of oblique incidence

Since in nearly all practical applications of noise control the incident sound field is not a normally incident plane acoustic wave, it is important to evaluate the performance of the PAM with strip masses and the proposed analytical model in the case of obliquely incident plane acoustic waves. This is particularly important, because the analytical model in section II has been derived under the assumption of spatially constant acoustic loading. For obliquely incident sound waves, this loading will, in general, not be constant in the xy-plane. Thus, the accuracy of the model needs to be evaluated for these cases. For this purpose, additional simulations have been performed with different values of the incidence angle θ_0 and the azimuth angle ϕ_0. The azimuth angle has been varied since PAM with strip masses are highly orthotropic and it may be possible that an oblique sound wave propagating in x-direction (perpendicular to the strips) can be transmitted differently than a wave propagating in y-direction (parallel to the strips). Since the analytical model relies on a homogenization at normal incidence, any possible influence of the azimuth angle ϕ_0 is neglected. Only the effect of the incidence angle θ_0 is taken into account via the cosine term in Equation 21.

Figure 7(a) compares three different simulation results with $\phi_0 = 0°$, 45°, and 90° to the analytical results ($\mathcal{C} = 0.046$) at an incidence angle of $\theta_0 = 30°$. For $\phi_0 = 0°$, the acoustic loading is varying only in the x-direction, while for 90° the loading spatially varies only in the y-direction. $\phi_0 = 45°$ is representative for an excitation where the sound pressure varies in both directions. Since all three simulation results are virtually the same, it can be concluded that the PAM with strip masses is not sensitive with respect to the azimuth angle of an obliquely incident acoustic wave. A possible explanation for this is the unit cell size of the PAM, which is—even at the highest frequency considered here—considerably smaller than the sound wave length. Therefore, the sound field exciting the PAM will be nearly uniform

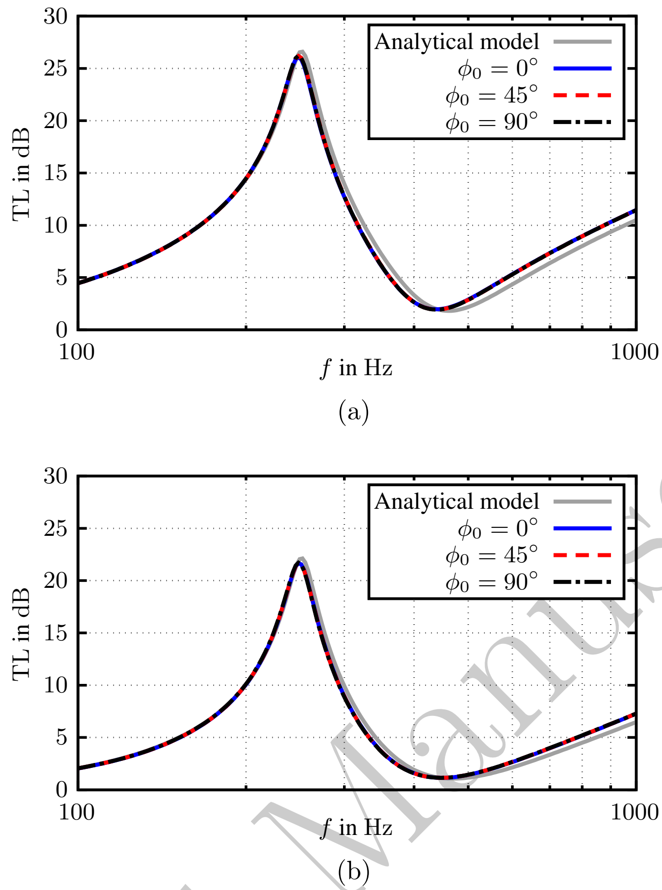

FIG. 7. (Color online) Comparison of analytical and numerical results for the oblique incidence sound transmission loss of the PAM. (a) $\theta_0 = 30°$. (b) $\theta_0 = 60°$.

(and thus very similar to normal incidence), even at grazing incidence. The comparison with the analytical model demonstrates that at oblique incidence the main characteristics of the PAM transmission loss (anti-resonance peak, resonance dip) are not changed under oblique incidence. Only the magnitude of the STL is reduced, which is well reflected by the $\cos\theta_0$ term in Equation 21.

Figure 7(b) shows the results for a higher incidence angle of $\theta_0 = 60°$. Also in this case there is no significant impact of ϕ_0 visible and the analytical model is in good agreement with the numerical simulations.

In summary, these results demonstrate that the performance of the PAM under oblique incidence is not significantly altered, except for the STL reduction due to the $\cos\theta_0$-dependence. The anti-resonances and resonances of the PAM remained unchanged and the analytical model yields good estimates of the PAM transmission loss at oblique incidence.

C. Effect of strip mass compliance

A central assumption in the analytical model is that the strip masses are rigid, compared to the bending stiffness of the baseplate. For applications of these PAM it is important to consider the limitations of this assumption, which can be violated, for example, when the strip masses are very thin and/or made of a soft material.

Simulations have been performed with different bending stiffnesses of the masses D_{M}. This has been achieved by changing the Young's modulus of the mass material E_{M}, so that all other parameters (mass, geometry, and mesh) remain unchanged. In the original configuration, the ratio of the mass bending stiffness to the baseplate bending stiffness is given by $D_{\mathrm{M}}/D_{\mathrm{b}} \approx 43000$. Figure 8 shows the simulation results for reduced mass bending stiffnesses down to $D_{\mathrm{M}}/D_{\mathrm{b}} = 50$. As the bending stiffness of the masses is reduced, it can be seen that the first anti-resonance of the PAM moves down to lower frequencies. This is because the overall stiffness inside the unit cell is reduced. For the case $D_{\mathrm{M}}/D_{\mathrm{b}} = 100$, an additional anti-resonance appears at around 350 Hz which becomes larger and shifted to lower frequencies when $D_{\mathrm{M}}/D_{\mathrm{b}}$ is further reduced. This new anti-resonance results from higher order modes of the PAM unit cell that are shifted within the frequency range of

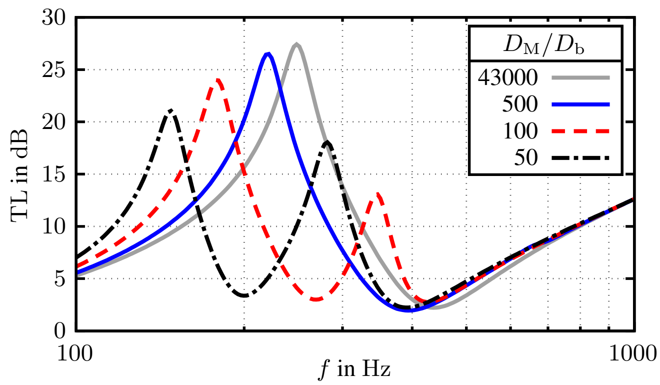

FIG. 8. (Color online) Numerical results for the normal incidence sound transmission loss of the PAM with different values for the mass bending stiffness D_{M}.

interest due do the reduced stiffening effect by the added masses. In general, the STL of these higher order anti-resonances is not much higher than the mass-law. However, in certain applications it could be useful to create multiple anti-resonances by using more compliant strip masses.

As a general recommendation for the validity of the rigid mass assumption in the analytical model, the results in Figure 8 indicate that the bending stiffness of the strip masses should be at least 1000 times higher than the baseplate bending stiffness. For example, if the elastic material properties of the masses and baseplate are similar, this would imply that the strip masses should be at least 10 times thicker than the baseplate.

IV. EXPERIMENTAL DEMONSTRATION

The experimental test sample was built based on the same unit cell geometry and material parameters for the baseplate and strip masses as in the numerical simulations (see section III). Figure 9(a) shows a photograph of the baseplate and two of the strip masses

(a)

(b)

FIG. 9. (Color online) Test sample and measurement setup for the experimental demonstration of the PAM with strip masses. (a) Detail view of the baseplate and attached strip masses. (b) Test sample mounted inside the transmission loss test window (view from the reverberation chamber).

attached to it. The overall size of the sample was $1\,\mathrm{m} \times 1.2\,\mathrm{m}$ in order to fit inside the transmission loss test window, see Figure 9(b). 17 PCV foam strip masses were attached to the PET baseplate using a thin double-sided tape. The contribution of the added mass due to the tape is negligible compared to the strip masses.

Additionally, a 1 mm thick glass fiber reinforced plastic (GFRP) plate with a surface mass density of $2\,\mathrm{kg\,m^{-2}}$ was also measured. This homogeneous plate with nearly the same mass as the PAM sample serves as a reference to compare with the STL of the PAM.

As shown in Figure 9(b), the samples were mounted inside a transmission window between a reverberation chamber (shown in the picture) and a hemi-anechoic chamber. The samples were fixed at the perimeter using clamps and foam rubber to minimize leakage and the transfer of vibrations over the window frame. In the reverberation chamber, a diffuse sound field was generated using an omnidirectional loudspeaker and a white noise signal resulting in an overall sound pressure level in the reverberation chamber of around 100 dB(Z). The measurement of the STL was performed in 1/12th-octave bands according to a modified ISO 15186-2 method: While, in the anechoic chamber, a sound intensity probe was used to measure the transmitted sound power, the incident sound power was estimated using a sound intensity measurement of the empty test window (Robin and Berry, 2016). This reduces the influence of non-diffusiveness of the excitation sound field on the measured STL, particularly at low frequencies.

For comparing the experimental data with the analytical results, the diffuse field STL has been calculated using

$$\mathrm{TL}_{\mathrm{diff}} = -10\,\mathrm{lg}\left(\frac{\int\limits_0^{\theta_{\max}} \tau\sin(\theta_0)\cos(\theta_0)\,\mathrm{d}\theta_0}{\int\limits_0^{\theta_{\max}} \sin(\theta_0)\cos(\theta_0)\,\mathrm{d}\theta_0}\right), \tag{29}$$

with the transmission coefficient $\tau = 10^{-\mathrm{TL}/10}$ and the limiting angle $\theta_{\max}$ has been estimated in previous experiments as $\theta_{\max} = 72^\circ$ (Langfeldt and Gleine, 2020b).

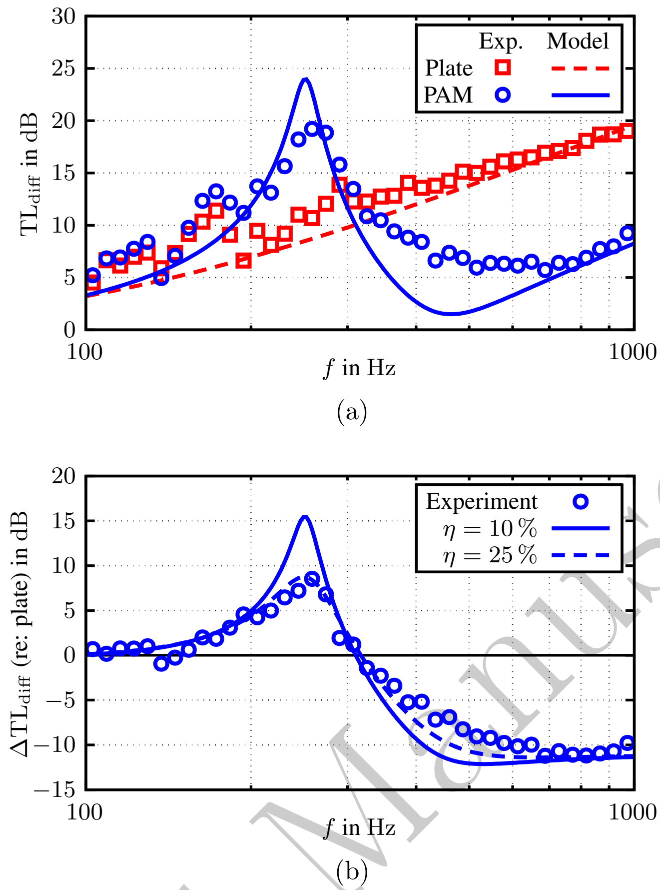

FIG. 10. (Color online) Comparison of analytical (curves) and experimental results (symbols) for the PAM and the nearly mass-equivalent homogeneous plate. (a) Diffuse incidence sound transmission loss. (b) Insertion loss (re: homogeneous plate) with a variation of the loss factor η in the analytical model.

The measured STL of the PAM and the homogeneous GFRP plate (symbols) are compared to the analytical results (curves) in Figure 10(a). In general, the agreement between the analytical and experimental results is good, especially taking into account the simplicity of the analytical model. In the measurements, the anti-resonance occurs at around 260 Hz, which is about 4 % higher than in the analytical model (251 Hz). This deviation is within acceptable limits, since uncertainties in the material properties of the PAM as well as the unit cell geometry typically also lie in this range. The measured maximum STL value is about 5 dB lower than in the analytical results. Also, the STL reduction at the first resonance of the PAM is not as distinct in the measurements. These systematic deviations can be explained by two separate effects, which are not taken into account in the analytical model: First, the experimental sample can exhibit increased losses due to damping in the double-sided tape attachment as well as the sample fixture at the transmission window frame, where foam rubber was used to prevent leaks. These damping mechanisms can exceed the inherent damping of the film and mass material. Second, the impact of inaccuracies in the placement of the masses can have an additional damping-like effect on the sound transmission loss of the PAM, as shown in (Langfeldt and Gleine, 2020a). Since the mass strips have been glued on manually and the PAM resonance frequency is proportional to $1/l^2$ (see Equation 27), small variations in the mass spacing l can lead to rather large changes in the modal properties of each PAM unit cell. A random sampling of l provided an estimate for the uncertainty of the mass spacing in the present experimental model of the PAM given by $l = (20.0 \pm 1.2)$ mm. From Equation 13 and Equation 23 it follows that the resulting uncertainties in the resonance and anti-resonance frequency are (447 ± 54) Hz and (251 ± 33) Hz, respectively. As shown in (Langfeldt and Gleine, 2020a), such manufacturing inaccuracies can therefore result in a smoothened STL curve of the PAM, similar to the effect of damping.

Finally, it should be noted that at very low frequencies the analytical model underestimates the measured STL values. The reason for this is the spatial windowing effect of the finite sized transmission window in the experiments, which is not taken into account in the analytical model. This effect can be eliminated for the most part, as shown in Figure 10(b), by calculating the insertion loss of the PAM $\Delta\mathrm{TL}_{\mathrm{diff}}$, compared to the homogeneous plate. In this case, the agreement between the analytical and experimental data is much better, except for the aforementioned smoothing of the anti-resonance peak and resonance dip. That, however, can be considered in the analytical model by increasing the loss factor η to, in this case, 25 % (see the dashed curve in Figure 10(b)). It should be noted that the modeling of damping using a constant loss factor strongly simplifies such a complex phenomenon (especially when glue layers, rubber foam seals, and manufacturing inaccuracies are present). While a good estimate for η can greatly improve the accuracy of the model, quantifying and modeling the damping of a PAM still is a challenge which should be subject to further investigations.

V. CONCLUSIONS

In this contribution a new type of plate-type acoustic metamaterials with significantly reduced complexity, as compared to previous PAM designs, has been presented. The proposed PAM employs strip masses attached to a baseplate in order to reduce the periodicity of the metamaterial unit cells to one dimension. An analytical model has been derived to estimate the modal properties of the PAM unit cell, enabling the direct calculation of the effective surface mass density m''_{eff} and sound transmission loss of the PAM. For large masses of the strips (compared to the baseplate mass), the analytical model has been further simplified yielding explicit expressions for the modal properties of PAM that can be directly employed in the initial design phase for applications of such PAM to noise control problems.

Numerical simulations have been performed to verify the analytical model. Using the simulations, it could also be demonstrated that the performance of the PAM is not affected by obliquely incident plane acoustic waves (except for the typical $\cos\theta_0$ dependence). The assumption of rigid strip masses (compared to the baseplate) in the analytical model has been shown to be reasonably accurate, as long as the bending stiffness of the masses is at least 1000 times higher than the bending stiffness of the baseplate. Finally, sound transmission loss measurements of a PAM with strip masses have been performed to demonstrate the performance of the PAM and the accuracy of the analytical model under diffuse field excitation and finite sized sample conditions.

The results presented herein will considerably improve the applicability of PAM to practical noise control problems: First, the simplified design reduces the manufacturing effort significantly, which is one of the major inhibiting factors for realizations of other, more complex acoustic metamaterials in an industrial scale. Secondly, the proposed analytical model yields, for the first time in the context of MAM and PAM, explicit expressions to directly estimate the vibro-acoustic performance of PAM with strip masses, without resorting to more complex analytical models or finite element simulations.

ACKNOWLEDGMENTS

This work has been performed under the framework of the German-Canadian joint research project New Acoustic Insulation Metamaterial Technology for Aerospace (NAIMMTA), funded by the Federal Ministry of Education and Research (grant number: 03INT504AB). The financial support is gratefully acknowledged by the authors.

Ang, L. Y. L., Koh, Y. K., and Lee, H. P. (**2018**). "Plate-type acoustic metamaterial with cavities coupled via an orifice for enhanced sound transmission loss," Appl. Phys. Lett. **112**(5), 051903, doi: 10.1063/1.5019602.

Ang, L. Y. L., Koh, Y. K., and Lee, H. P. (**2019**). "Plate-type acoustic metamaterials: Evaluation of a large-scale design adopting modularity for customizable acoustical performance," Appl. Acoust. **149**, 156–170, doi: 10.1016/j.apacoust.2019.01.027.

Antonakakis, T., and Craster, R. V. (**2012**). "High-frequency asymptotics for microstructured thin elastic plates and platonics," Proc. R. Soc. A **468**(2141), 1408–1427, doi: 10.1098/rspa.2011.0652.

Chen, Y., Huang, G., Zhou, X., Hu, G., and Sun, C.-T. (**2014**). "Analytical coupled vibroacoustic modeling of membrane-type acoustic metamaterials: Plate model," J. Acoust. Soc. Am. **136**(6), 2926–2934, doi: 10.1121/1.4901706.

Craster, R. V., Kaplunov, J., and Pichugin, A. V. (**2010**). "High-frequency homogenization for periodic media," Proc. R. Soc. A **466**(2120), 2341–2362, doi: 10.1098/rspa.2009.0612.

de Melo Filho, N., Van Belle, L., Claeys, C., Deckers, E., and Desmet, W. (**2019**). "Dynamic mass based sound transmission loss prediction of vibro-acoustic metamaterial double panels applied to the mass-air-mass resonance," J. Sound Vib. **442**, 28–44, doi: 10.1016/j.jsv.2018.10.047.

Fokin, V., Ambati, M., Sun, C., and Zhang, X. (**2007**). "Method for retrieving effective properties of locally resonant acoustic metamaterials," Phys. Rev. B **76**, 144302, doi: 10.

1103/PhysRevB.76.144302.

Huang, T.-Y., Shen, C., and Jing, Y. (**2016**). “Membrane- and plate-type acoustic metamaterials,” J. Acoust. Soc. Am. **139**(6), 3240–3250, doi: 10.1121/1.4950751.

Kurtze, G. (**1959**). “Light-weight walls with high transmission loss,” Acta Acust. united Ac. **9**(6), 441–445.

Langfeldt, F., and Gleine, W. (**2019**a). “Improved sound transmission loss of glass wool with acoustic metamaterials,” in *Proceedings of the 26th International Congress on Sound and Vibration*, Montréal.

Langfeldt, F., and Gleine, W. (**2019**b). “Membrane- and plate-type acoustic metamaterials with elastic unit cell edges,” J. Sound Vib. **453**, 65–86, doi: 10.1016/j.jsv.2019.04.018.

Langfeldt, F., and Gleine, W. (**2020**a). “Impact of manufacturing inaccuracies on the acoustic performance of sound insulation packages with plate-like acoustic metamaterials,” SAE Technical Paper 2020-01-1562, doi: 10.4271/2020-01-1562.

Langfeldt, F., and Gleine, W. (**2020**b). “Optimizing the bandwidth of plate-type acoustic metamaterials,” J. Acoust. Soc. Am. **148**(3), 1304–1314, doi: 10.1121/10.0001925.

Liu, C. R., Wu, J. H., Lu, K., Zhao, Z. T., and Huang, Z. (**2019**). “Acoustical siphon effect for reducing the thickness in membrane-type metamaterials with low-frequency broadband absorption,” Appl. Acoust. **148**, 1–8, doi: 10.1016/j.apacoust.2018.12.008.

Liu, Y., and Du, J. (**2019**). “Vibroacoustic characteristics and sound attenuation analyses of a duct–membrane system coupled with strip masses,” J. Vib. Control **25**(23-24), 2910–2920, doi: 10.1177/1077546319873459.

Maysenhölder, W. (**1998**). "Sound transmission through periodically inhomogeneous anisotropic thin plates: Generalizations of cremer's thin plate theory," Acta Acust. united Ac. **84**(4), 668–680.

Maysenhölder, W. (**2004**). "Bending-Wave Energy Propagation in Inhomogeneous Thin Plates and Membranes," in *Proceedings of Inter-Noise 2004*, Prague, pp. 4084–4091.

Mei, J., Ma, G., Yang, M., Yang, Z., Wen, W., and Sheng, P. (**2012**). "Dark acoustic metamaterials as super absorbers for low-frequency sound," Nat. Commun. **3**, doi: 10.1038/ncomms1758.

Naify, C. J., Chang, C.-M., McKnight, G., and Nutt, S. (**2011**). "Transmission loss of membrane-type acoustic metamaterials with coaxial ring masses," J. Appl. Phys. **110**(12), 124903, doi: 10.1063/1.3665213.

Naify, C. J., Chang, C.-M., McKnight, G., and Nutt, S. R. (**2012**). "Scaling of membrane-type locally resonant acoustic metamaterial arrays," J. Acoust. Soc. Am. **132**(4), 2784–2792, doi: 10.1121/1.4744941.

Rao, S. S. (**2007**). *Vibration of Continuous Systems* (John Wiley & Sons, Ltd, Hoboken).

Robin, O., and Berry, A. (**2016**). "Alternative methods for the measurement of panel transmission loss under diffuse acoustic field excitation," in *Proceedings of Inter-Noise 2016*, Hamburg, pp. 3340–3358.

Terroir, A., Schwan, L., Cavalieri, T., Romero-García, V., Gabard, G., and Groby, J.-P. (**2019**). "General method to retrieve all effective acoustic properties of fully-anisotropic fluid materials in three dimensional space," J. Appl. Phys. **125**(2), 025114, doi: 10.1063/1.5066608.

Varanasi, S., Bolton, J. S., and Siegmund, T. (**2017**). "Experiments on the low frequency barrier characteristics of cellular metamaterial panels in a diffuse sound field," J. Acoust. Soc. Am. **141**(1), 602–610, doi: 10.1121/1.4974257.

Ventsel, E., and Krauthammer, T. (**2001**). *Thin Plates and Shells: Theory, Analysis, and Applications* (Marcel Dekker, Inc., New York).

Wang, X., Chen, Y., Zhou, G., Chen, T., and Ma, F. (**2019**). "Synergetic coupling large-scale plate-type acoustic metamaterial panel for broadband sound insulation," J. Sound Vib. **459**, 114867, doi: 10.1016/j.jsv.2019.114867.

Xiao, Y., Cao, J., Wang, S., Guo, J., Wen, J., and Zhang, H. (**2021**). "Sound transmission loss of plate-type metastructures: Semi-analytical modeling, elaborate analysis, and experimental validation," Mech. Syst. Signal Process. **153**, 107487, doi: 10.1016/j.ymssp.2020.107487.

Xiao, Y., Wen, J., and Wen, X. (**2012**). "Sound transmission loss of metamaterial-based thin plates with multiple subwavelength arrays of attached resonators," J. Sound Vib. **331**(25), 5408–5423, doi: 10.1016/j.jsv.2012.07.016.

Yang, M., Ma, G., Wu, Y., Yang, Z., and Sheng, P. (**2014**). "Homogenization scheme for acoustic metamaterials," Phys. Rev. B **89**(6), doi: 10.1103/PhysRevB.89.064309.

Yang, Z., Dai, H. M., Chan, N. H., Ma, G. C., and Sheng, P. (**2010**). "Acoustic metamaterial panels for sound attenuation in the 50-1000 Hz regime," Appl. Phys. Lett. **96**(4), doi: 10.1063/1.3299007.

Yang, Z., Mei, J., Yang, M., Chan, N. H., and Sheng, P. (**2008**). "Membrane-type acoustic metamaterial with negative dynamic mass," Phys. Rev. Lett. **101**, 204301, doi: 10.1103/

PhysRevLett.101.204301.